Amplifying time-harmonic thermal signal in spinning lock-in thermography

Check for updates

Yanxiang Wang[1,2,3], Dong Wang[1,2,3], Xiaochang Xing[1,2,3], Pei-Chao Cao[1,2,3], Qiang-Kai-Lai Huang[1,2,3], Hao-Ran Yan[1,2,3], Hongsheng Chen [1,2,3] ✉ & Ying Li [1,2,3] ✉

Time-harmonic thermal signals (or thermal waves) are widely used in non-destructive testing (NDT), particularly in lock-in thermography (LIT), an infrared-based technique for material evaluation. LIT relies on modulated thermal signals to probe material properties and detect structural defects with high sensitivity. However, traditional LIT methods are often limited to static heat sources or samples, restricting their use in dynamic scenarios. Moreover, very few studies have focused on the characteristics of thermal waves during their propagation, which is crucial for the understanding of dynamic heat transfer. This work presents a dynamic model for LIT that emphasizes the propagation characteristics of time-harmonic thermal signals. Through theoretical analysis, simulation modeling, and experimental measurements, we investigate the propagation behaviors of these thermal signals in double-layer and triple-layer models under various conditions. Our findings reveal the amplitude amplification effect of thermal signals in time-harmonic heat transfer, enabling thermal analysis in moving materials or mechanical structures, and show the potential application in NDT. This may lay a foundation for the development of advanced thermal-wave based diagnostic methods and the exploration of novel heat transfer mechanisms in dynamic systems.

Non-destructive testing, namely the process of evaluating and inspecting materials, components, or systems without causing any damage or alteration to their structure or functionality, aims to detect defects, assess material properties, and monitor the condition of components during their lifecycle[1,2]. Based on the material properties being tested, such as metals, plastics, ceramics, composites, a wide range of NDT methods have been applied, such as ultrasonic testing (UT), X-ray and radiography, eddy current testing (ECT) and acoustic emission (AE) and thermography[3-5]. Commonly-used thermography includes steady-state thermography (SST, also called as passive thermography), pulsed thermography (PT) and lock-in thermography (LIT). SST involves capturing and analyzing the natural thermal radiation emitted by an object without applying any external heat source. It relies solely on the thermal energy that is already present in the environment or the object itself. PT and LIT, often considered as active thermography because of evaluation of dynamic temperature changes, are powerful NDT methods that measures the surface temperature distribution of materials[6]. They are especially valuable for detecting surface and subsurface defects by analyzing thermal responses to external stimuli.

Significant progress has been made in the study of wave-like heat transfer in thermal meta materials[7-17], including thermal wave cloak[18,19],

thermal wave rectification[20-22], heat pump[23-26], non-reciprocal thermal metadevices[27-29], coherent perfect absorption[30], skin effect[31-34]. These advances have demonstrated the flexibility of thermal metamaterials in controlling thermal wave signals. LIT exploits modulated thermal waves to detect material properties and structural defects, offering advantages such as high sensitivity and spatial resolution[35-42]. Traditionally, LIT utilizes modulated thermal waves to probe the properties of materials and detect internal defects. The principle behind LIT involves applying a periodic thermal excitation (often sinusoidal thermal wave) to the surface of a material, typically through infrared radiation[43]. This excitation induces a corresponding periodic temperature distribution on the material's surface, which is influenced by both the material's thermal properties and the presence of defects.

In LIT, the sample is subjected to a modulated heat source, which induces a periodic fluctuation in the surface temperature. The thermal waves propagate into the material, and the amplitude and phase of the surface temperature variation are affected by factors such as material heterogeneity, internal defects, and boundary conditions. These temperature variations are then captured by an infrared camera, which records the thermal response over time. The key advantage of LIT is its ability to extract

[1]International Joint Innovation Center, The Electromagnetics Academy at Zhejiang University, Zhejiang University, Haining, 314400, China. [2]State Key Laboratory of Extreme Photonics and Instrumentation, Zhejiang Key Laboratory of Intelligent Electromagnetic Control and Advanced Electronic Integration, Zhejiang University, Hangzhou, 310027, China. [3]Jinhua Institute of Zhejiang University, Zhejiang University, Jinhua, 321099, China. ✉e-mail: hansomchen@zju.edu.cn; eleying@zju.edu.cn

both amplitude and phase information from the thermal response, which provides insight into the material's internal structure. The combined analysis of both the amplitude and phase shift between the applied thermal modulation and the measured surface temperature allows for accurate localization and characterization of defects within the material. Signal processing techniques, such as Fourier transforms[44], along with various modulation methods, are employed to enhance the signal-to-noise ratio (SNR, also referred to as the contrast-to-noise ratio, CNR)[45] and to extract the defect-related information from the corresponding thermal response.

Multiple approaches are introduced to thermally excite the material to be measured, with LIT relying on continuous thermal waves to inject energy into the detected object[46]. Among these, halogen lamps offer several advantages like low cost, broad spectral range, wide application versatility, and high-power output, making them a popular choice as thermal excitation sources in various detection systems. Their ability to provide a consistent and uniform light output further enhances their utility in thermographic applications, especially when large-area excitation is required. Reference [47] applies the halogen lamps to reconstruct three-dimensional defect morphology. Laser is also a commonly-used heat source to get more uniform illumination[48]. Other methods, such as ultrasonic, electromatic eddy current, and microwave, are also adopted in related works[49–51]. As for the detected sample, traditional LIT mostly focuses static scenarios, where the infrared camera, the object and heat source remain fixed during the entire inspection. Recent advances include scanning thermography deployed by laser arrays (laser arrays scan thermography, LAsST), whose specimen is given a variable speed scanned by a fixed laser array[52].

Despite its effectiveness, it is noticeable that in the process of using traditional LIT for NDT of samples, both amplitude and phase characteristics are of significant interest as they allow for the convenient localization of defect points. However, in the meantime, analysis of the propagation characteristics of time-harmonic thermal signals has received relatively less attention. Also, constrained by its static nature, where the heat source, the detected sample, and the infrared camera remain stationary, thereby limiting its broader applicability, especially when part or all of these three components are in motion. To overcome the mentioned limitations of static nature, and in order to gain a comprehensive understanding of the transmission characteristics of time-harmonic thermal fields throughout the entire propagation process, here we introduce a dynamic framework based on continuous thermal waves as well as rotating samples. By utilizing a thermal analog of scattering theory[15,20,27,30], we are able to amplify thermal signals under resonant conditions, achieving a significant increase in temperature intensity. Our theoretical framework explores the interplay between thermal wave propagation and dynamic LIT scenarios. Specifically, we examine a situation where a rotating unit generates thermal waves that are conductively transmitted to the sample. This method has been validated through a combination of theoretical analysis and finite-element simulations, demonstrating the potential to amplify thermal signals under optimal condition than that of static situation. This resonant-like amplification effect has critical implications for improving the efficiency of infrared NDT of material science. It not only paves the way for more efficient LIT techniques but also broadens the scope of thermal wave research to dynamic systems or other thermal metamaterials.

Results
Scattering theory (double-layer model)

We begin by considering a theoretical model consisting of two independent rings with their centers aligned along the same axis. We postulate that the medium is homogeneous in the radial direction and the cylinder has a small thickness (as shown in Fig. 1a, b). For the sake of clear and general explanation, we assume that the two annuli are stacked along the z-axis. Consequently, the following temperature field function of the z-direction can be expressed as:

$$T(z, \omega, t) = T_0 + (B_+ e^{ikz} + B_- e^{-ikz})e^{-i\omega t} \tag{1}$$

Here, T_0 is the reference temperature, analogous to the direct current component in circuits, while B_+ and B_- represent the ingoing and outgoing

Fig. 1 | Schematics of the double-layer and triple-layer model. The base of the bottom layer provides continuous sinusoidal thermal wave, while the first layer acts as a convective medium whose angular velocity modulates the temperature amplitude on its top surface. **a** Diagrammatic figure. **b** Side view of the double-layer structure. For the triple-layer model, the top (corresponding to the second layer in (**c**)) layer can be seen as a device under test, in this model, where the combined angular velocities of both the first and second layers simultaneously modulate the sample's thermal response. **c** Diagrammatic figure and **d** Side view of the triple-layer structure. **e** temperature profile by flattening the circumference. Letters b, d and R are geometric parameters: $b = 0.005$ m, $d = 0.022$ m, $R = 0.055$ m. $z = 0$ represents the coordinate origin. ω is the thermal frequency. Ω and $\Omega_i(i = 1, 2)$ denote corresponding angular velocities. When viewed from the origin towards the negative direction of the z-axis, a clockwise rotation corresponds to a positive value.
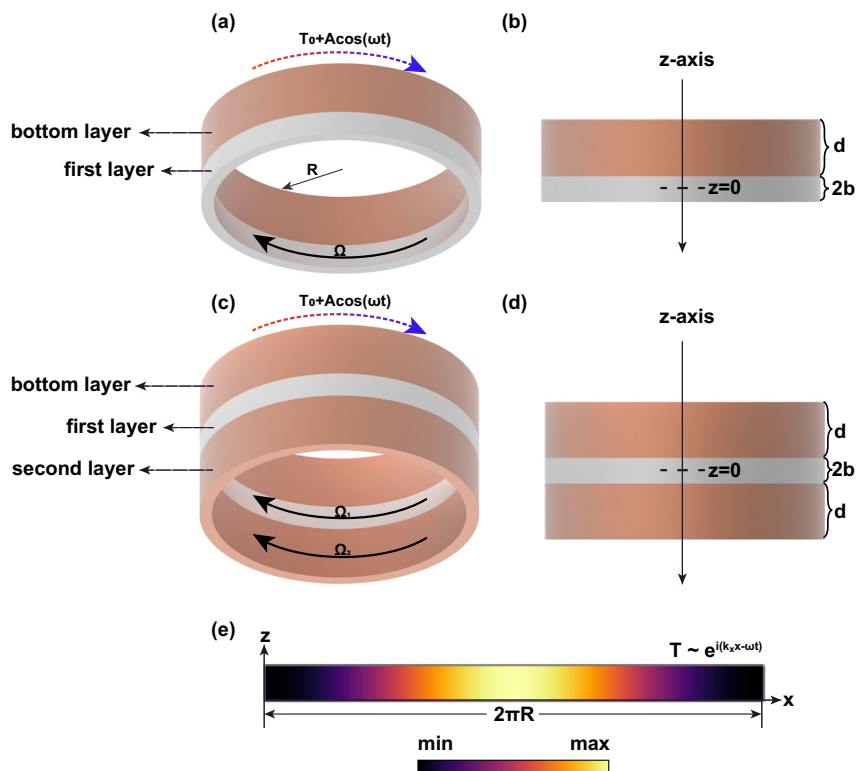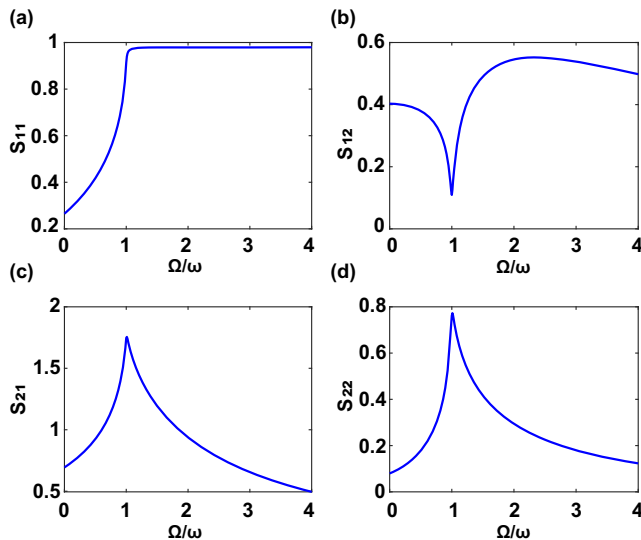
Fig. 2 | Scattering characteristics of the double-layer model. Here $\omega = \frac{\pi}{4}$ rad s^{-1}. The bule solid lines are the modulus of elements in the scattering matrix with respect to different Ω. **a** S_{11}, **b** S_{12}, **c** S_{21} and **d** S_{22}.

signals, respectively. Additionally, k is the wave number, ω is the thermal frequency, and t denotes time.

According to Fourier's law in heat transfer, macroscopic heat conduction is governed by the equation $q = -\kappa \cdot \nabla T$, where q is the heat flux density, T is the temperature and κ is the thermal conductivity tensor. Taking into account energy conservation, the temperature field satisfies $\rho c_p \frac{\partial T(\boldsymbol{r},t)}{\partial t} = \nabla \cdot (\kappa \cdot \nabla T(\boldsymbol{r}, t)) + g(\boldsymbol{r}, t)$, where $\boldsymbol{r}$ is the position vector, $g(\boldsymbol{r}, t)$ is the rate of energy generation, ρ and c_p represent mass density and specific heat capacity at constant pressure, respectively. When convection with velocity $\boldsymbol{v}$ is introduced, the governing equation is transformed into the convection-diffusion equation $\rho c_p \frac{\partial T(\boldsymbol{r},t)}{\partial t} = \nabla \cdot (\kappa \cdot \nabla T(\boldsymbol{r}, t)) - \rho c_p \boldsymbol{v} \cdot \nabla T(\boldsymbol{r}, t) + g(\boldsymbol{r}, t)$.

The temperature field in this work adheres to the governing equations as follows:

$$\begin{cases} \frac{\partial T_c}{\partial t} = D_c \frac{\partial^2 T_c}{\partial x^2} + D_c \frac{\partial^2 T_c}{\partial z^2}, z \le z_1, \ 0 \le x \le 2\pi R \\ \frac{\partial T_r}{\partial t} = D \frac{\partial^2 T_r}{\partial x^2} - v \frac{\partial T_r}{\partial x} + D \frac{\partial^2 T_r}{\partial z^2}, z_1 \le z \le z_2, 0 \le x \le 2\pi R \end{cases} \quad (2)$$

The distribution equations for T_c and T_r are given by:

$$\begin{cases} T_c = T_0 + \left[B_{c+} e^{ik_c z_1} e^{ik_c(z-z_1)} + B_{c-} e^{-ik_c z_1} e^{-ik_c(z-z_1)} \right] e^{ik_x x - i\omega t}, \\ \quad z \le z_1, 0 \le x \le 2\pi R \\ T_r = T_0 + \left[B_{r+} e^{ik_r z} + B_{r-} e^{-ik_r z} \right] e^{ik_x x - i\omega t}, \\ \quad z_1 \le z \le z_2, 0 \le x \le 2\pi R \end{cases} \quad (3)$$

Here T_c and T_r denote the temperature fields, where the subscripts c and r correspond to the bottom and first layer, respectively. The thermal diffusivities are defined as $D_c = \frac{\kappa_c}{\rho_c c_c}$ and $D = \frac{\kappa_r}{\rho_r c_r}$. The linear velocity of the first layer is $v = \Omega R$, where Ω is the convective velocity and R represents the radius of the concentric annulus. The position coordinates along the z-axis are z_1 and z_2 with $z_1 = -b$ and $z_2 = b$, and the respective thickness of the bottom and first layer is d and $2b$ (Fig. 1).

In theoretical analysis, we assume that all physical parameters exhibit isotropy and homogeneity, and the thickness of the selected ring is relatively small. It is reasonable to neglect the radial temperature difference. A sinusoidal temperature distribution at (r, θ) of the bottom layer follows the function $T(r, \theta, \omega) = T_0 + A\cos(\theta - \omega t) = T_0 + A\cos(k_x x - \omega t)$,

where A represents the temperature amplitude and the x-axis is defined by flattening the circumference with the conditions $x \sim x + 2\pi R$, $k_x = \frac{2\pi}{2\pi R} = \frac{1}{R}$. Figure 1e depicts the periodic temperature profile. In this case, the wavelength of a thermal wave in Cartesian coordinates exactly corresponds to the polar angle of 2π radians in polar coordinates.

The first layer is regarded as a convective medium rotating at Ω. The temperature distribution follows a pattern similar to that of the base of the bottom layer, with only a difference in the oscillating amplitude. Specifically, we are primarily interested in the amplitude of such wave-like heat transfer in this work.

By substituting the temperature waveform (Eq. 3) into the governing equation (Eq. 2), we have the following dispersion relationship:

$$\begin{cases} k_c^2 + k_x^2 = \frac{i\omega}{D_c} \\ k_r^2 + k_x^2 = \frac{i(\omega - \Omega)}{D} \end{cases} \quad (4)$$

with the boundary condition ($h = b + d$, $z_1 = -b$, $z_2 = b$)

$$\begin{cases} T_c(z_1) = T_r(z_1) \\ \kappa_c \frac{\partial T_c}{\partial z}\big|_{z=z_1} = \kappa_r \frac{\partial T_r}{\partial z}\big|_{z=z_1} \end{cases} \quad (5)$$

Rewrite the relation into matrix form:

$$\begin{pmatrix} 1 & 1 \\ 1 & -1 \end{pmatrix} \begin{pmatrix} B_{c+} e^{ik_c(-b)} \\ B_{c-} e^{-ik_c(-b)} \end{pmatrix} = \begin{pmatrix} e^{-ik_r b} & e^{ik_r b} \\ \frac{\kappa_r k_r}{\kappa_c k_c} e^{-ik_r b} & -\frac{\kappa_r k_r}{\kappa_c k_c} e^{ik_r b} \end{pmatrix} \begin{pmatrix} B_{r+} \\ B_{r-} \end{pmatrix} \quad (6)$$

Additionally, to calculate the amplitude terms B_{c+}, B_{c-}, B_{r+}, B_{r-}, auxiliary equation (Eq. 7) is combined with (Eq. 5):

$$\begin{cases} B_{c+} e^{ik_c(-h)} + B_{c-} e^{-ik_c(-h)} = A \\ B_{r+} e^{ik_r b} - B_{r-} e^{-ik_r b} = 0 \end{cases} \quad (7)$$

Then we simplify the terms $B_{c+} e^{ik_c z_1}$, $B_{c-} e^{ik_c z_2}$ and $\frac{\kappa_r k_r}{\kappa_c k_c}$ into A_1, B_1 and γ, define the transfer matrix M as $\begin{pmatrix} B_{r+} \\ B_{r-} \end{pmatrix} = M \begin{pmatrix} A_1 \\ B_1 \end{pmatrix} = \begin{pmatrix} M_{11} & M_{12} \\ M_{21} & M_{22} \end{pmatrix} \begin{pmatrix} A_1 \\ B_1 \end{pmatrix}$, scattering matrix S as $\begin{pmatrix} B_1 \\ B_{r+} \end{pmatrix} = S \begin{pmatrix} A_1 \\ B_{r-} \end{pmatrix} = \begin{pmatrix} S_{11} & S_{12} \\ S_{21} & S_{22} \end{pmatrix} \begin{pmatrix} A_1 \\ B_{r-} \end{pmatrix}$

$$M = \frac{1}{2\gamma} \begin{pmatrix} (\gamma + 1) e^{ik_r b} & (\gamma - 1) e^{ik_r b} \\ (\gamma - 1) e^{-ik_r b} & (\gamma + 1) e^{-ik_r b} \end{pmatrix} \quad (8)$$

$$S = \begin{pmatrix} \frac{1-\gamma}{1+\gamma} & \frac{2\gamma}{1+\gamma} e^{ik_r b} \\ \frac{2}{1+\gamma} e^{ik_r b} & \frac{\gamma-1}{\gamma+1} e^{2ik_r b} \end{pmatrix} \quad (9)$$

Thus far, we are able to obtain the scattering characteristics by sweeping ω and Ω to calculate the temperature waveform and corresponding amplitude. Similar to classical scattering theory, the thermal scattering elements S_{ij} represent the ratio of the thermal signal transmitted from port j to port i. In this work the two-port system is described in terms of ingoing and outgoing components. Typically, the off-diagonal components, namely S_{12} and S_{21}, signify the transmission coefficients, whereas the diagonal (S_{11} and S_{22}) stand for the reflection coefficients. When the condition $S_{12} \neq S_{21}$ holds, the double-layer model exhibits nonreciprocity. Figure 2 depicts the modulus of the corresponding elements, which are obtained by sweeping Ω with fixed ω.

From Fig. 2, it is clearly shown that when Ω approaches ω, the propagation characteristics corresponding to the four parameters undergo a

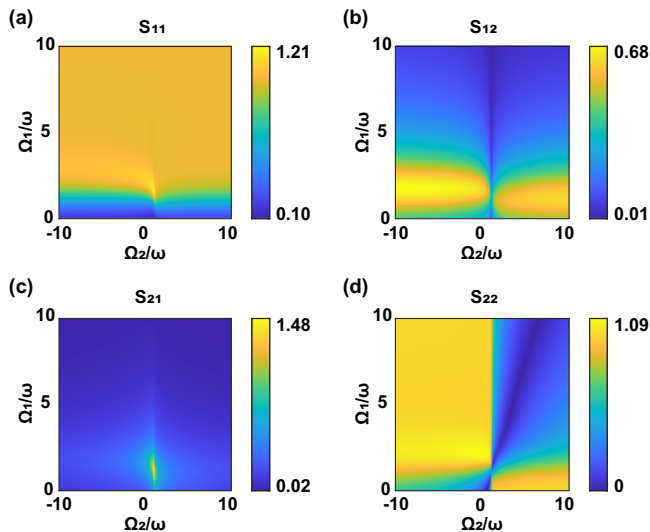**Fig. 3 | Scattering characteristics of the triple-layer model.** Here $\omega = \frac{\pi}{4}$ rad s^{-1}. The rotation direction of the target is defined such that $\Omega_i (i = 1, 2)$ is positive when the rotation is clockwise, and negative when the rotation is counterclockwise. The four plots correspond to the modulus of the scattering elements. **a** S_{11}, **b** S_{12}, **c** S_{21} and **d** S_{22}.

noticeable transition. From Fig. 2b, c, it can be indicated that the system exhibits significant forward-transmission performance at this specific frequency. This could imply that the system is well-optimized for transmitting signals from port 1 to port 2. On the other hand, S_{12} represents the reverse-transmission coefficient, which suggests that the system has strong isolation in the reverse direction.

The scattering elements can be interpreted from both mathematical and physical perspectives. Mathematically in general, they arise from the combined effect of γ and $e^{ik_r b}$ (Supplementary Fig. 1). The complex γ represents the ratio of two complex wave vectors. The real part (Supplementary Fig. 1a) reflects the phase synchronization: before the critical point, the decreasing real part indicates progressive phase matching between thermal waves in the two rings, achieving full synchronization beyond this point. The imaginary part (Supplementary Fig. 1b) governs attenuation characteristics. After the critical point, the attenuation of k_r exhibits significantly stronger attenuation than k_x. For $|S_{11}|$, its magnitude is jointly governed by two factors: system energy loss and convective-induced wave vector matching at the boundary. Beyond the phase-transition point, the real part of γ approaches zero, indicating significant wave vector magnitude disparity. This drives $|S_{11}| \rightarrow 1$ due to enhanced backscattering. Concurrently, the determinant of S attains large values post-transition (Supplementary Fig. 1e), confirming minimal system energy loss.

The magnitude $|S_{21}|$ depends on both $|\gamma|$ and $|e^{ik_r b}|$. Given the persistent positivity of real part of γ throughout the frequency range, maximum $|S_{21}|$ requires simultaneous minimization of $|\gamma|$ and maximization of $|e^{ik_r b}|$. Such conditions meet at the phase-transition point (Supplementary Fig. 1c, d). Conversely, $|S_{12}|$ correlates positively with $|\gamma|$, resulting in its minimum value at this point.

Finally, $|S_{22}|$ derives from $|S_{11}| \cdot |e^{2ik_r b}|$. Its peak occurs at the phase-transition point where the product of these terms maximizes.

The appearance of scattering elements greater than 1 might be puzzling. To clarify, the transmission coefficient presented here corresponds to the amplitude of the temperature field, with the spatial decay factor being removed. Moreover, the amplitude of the temperature field does not directly represent energy; rather, energy is determined by the temperature gradient multiplied by system-specific parameters. This is fundamentally different from wave systems, where energy is typically proportional to the square of the field amplitude.

To further understand the resonant-like heat transfer characteristics, we calculate a broader range of ω and Ω, as shown in Supplementary Fig. 2. The four subfigures all exhibit linear resonance relationship, which only depends on these two angular velocities, not on material parameters (Supplementary Fig. 3).

Scattering theory (triple-layer model)
To better understand the scattering characteristics and the potential to be applied in LIT where the device under test is in motion. Next, we derive a triple-layer model (corresponding to Fig. 1c, d). The mere difference is that an extra layer (i.e., the second layer) is added on top with another independent angular velocity Ω_2 to meet dynamic requirements. By employing an analogous derivation process, the propagation characteristics of the triple-layer model are obtained. The transmission coefficient S_{21} is $\frac{2\gamma_2}{(\gamma_1 + \gamma_2)\cos(2k_r b) - i(\gamma_1\gamma_2 + 1)\sin(2k_r b)}$, which is dependent on ω, Ω_1 and Ω_2, where $\gamma_1 = \frac{\kappa_r k_r}{\kappa_{c1} k_{c1}}$, $\gamma_2 = \frac{\kappa_r k_r}{\kappa_{c2} k_{c2}}$. Subscripts c_1, r, c_2 correspond to the bottom, first and second layer. We keep ω constant, sweeping Ω_1, Ω_2 to give out the modulus (Fig. 3) and symmetric results (Supplementary Fig. 4). For detailed derivation process, see Supplementary Note 1.

Simulation of the double-layer model
We firstly construct a double-layer concentric ring and use the heat transfer module to conduct our research. In the bottom layer, the temperature distribution adheres to the distribution of $T = T_0 + A\cos(k_x x - \omega t)$. The measured data represents the temporal temperature variation at a fixed position on the top surface of the first layer during one complete period. The temperature amplitude under current conditions is determined by calculating half the difference between the maximum and minimum temperature values.

Experimental verification of the double-layer model
Firstly, we put forward an experimental scheme to design time-harmonic heat source. A copper plate is placed in close contact with the bottom layer, with its two terminals subjected to different fixed temperatures: hot end T_h, and cold end T_c. Consequently, a fixed temperature boundary is set, thus forming a temperature gradient. Then a rotational angular velocity (thermal frequency) ω is applied. As a result, the temperature distribution of the bottom layer approximates the temperature distribution $T(\theta, \omega, t) = T_0 + \frac{T_h - T_c}{L} R\cos(\theta - \omega t)$, with L being the plate length. A stepper motor is implemented to control the copper plate to ensure that the temperature distribution is consistent with our simulation (Fig. 4a–c). During experimental operation, the measuring position is the temperature data at a point (r, θ) of the first layer. Theoretical analysis, simulation calculation and experiment results are shown in Fig. 4d. It is clearly illustrated that there exists a resonant-like heat transfer in the double-layer model, since the amplification effect is reflected in the comparison between the amplitude under resonant condition and the amplitude at static condition (2.50 K at resonant condition versus 1.06 K at static condition in the experiment). As the thermal wave propagates, it retains its original attenuation characteristics, as shown in Fig. 4d, where the amplitude remains smaller than the input amplitude.

Simulation of the triple-layer model
For ease of illustration without loss of generality, in the triple-layer simulation we give the first and the second layer the same physical parameters. Similarly, we fixed ω, then sweep Ω_1, Ω_2 to derive corresponding temperature amplitude (Fig. 5a). Such amplification effect is reflected by the amplitude of 21.64 K at resonant condition versus 1.95 K at static condition in the simulation (Fig. 5b).

Conclusion
In this work, we propose an amplification effect of time-harmonic temperature field under spinning lock-in thermography, and verified the
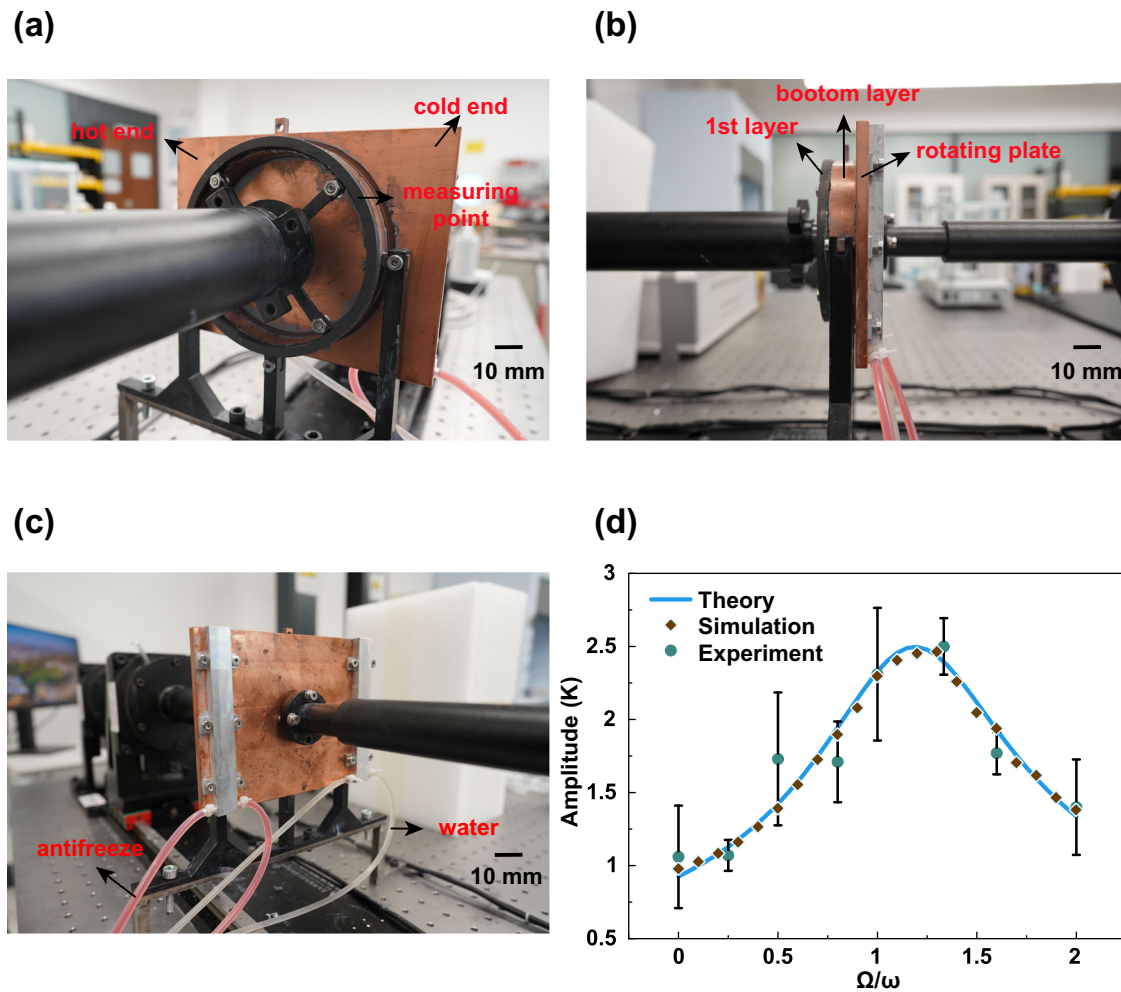
Fig. 4 | Photograph of experimental setup and corresponding results. a Front view. **b** Side view. **c** Back view. **d** Theoretical, simulation and experimental results. Light blue solid line represents the theoretical results. Brown scatter points represent the simulation results. Green scatter points with error bars represent the experimental data. (Scale bar: 10 mm, error bar: sum of standard deviation of peak and valley value in one period).

Fig. 5 | Theory and simulation results of the triple-layer model. Here $\omega = \frac{\pi}{4}$ rad s^{-1} **a** Temperature amplitude of varied Ω_1 and Ω_2. **b** Derived amplitude of theoretical results (light blue solid line with cyan triangles) and corresponding simulation results (brown scatter points).
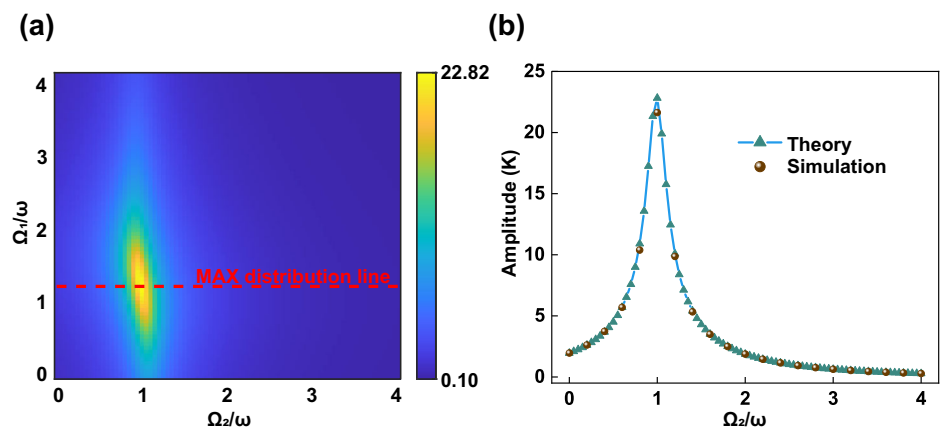
conclusion by theoretical calculation, simulation analysis and experiment. For the double-layer model, the transmission coefficient S_{21} consistently reaches its maximum value at the point where $\omega = \Omega$. However, it is noted that the sample's amplitude is influenced by the superposition of forward and backward waves, both of which depend on ω and Ω. As a result, when the amplitude attains its maximum, there is a slight offset in Ω from the

point $\omega = \Omega$. And as for the triple-layer model, both the transmission coefficient S_{21} and the maximum temperature amplitude occur at $\Omega_2 = \omega$. Near $\Omega_2 = \omega$, perturbation in Ω_2 have a substantial impact on the temperature amplitude, so it is possible to use the temperature amplitude characteristic for frequency detection and analysis with this effect. Also, in these two spinning lock-in thermography models, we calculate the

transmission coefficient modulus S_{21} and temperature amplitude versus material parameters (Supplementary Figs. 5 and 6). Moreover, since the material parameters are all related to the temperature amplitude, and we carry out artificially arbitrary structures in Supplementary Information (Supplementary Figs. 7 and 8), such resonant amplitude is significantly larger than that of static state. Our findings suggest that the results of this work could be applied to dynamic infrared nondestructive testing and are also expected to design novel dynamic thermal metamaterials.

Methods
Parameters (double-layer)
$T_0 = 298.15$ K, $A = 5$ K, $b = 0.005$ m, $d = 0.022$ m, $R = 0.055$ m, $\kappa_c = 310$ W m^{-1} K^{-1}, $\rho_c = 8900$ kg m^{-3}, $c_c = 390$ J kg^{-1} K^{-1}, $\kappa_r = 100$ W m^{-1} K^{-1}, $\rho_r = 7900$ kg m^{-3}, $c_r = 460$ J kg^{-1} K^{-1}, $\omega = \frac{\pi}{4}$ rad s^{-1}. Experimental parameters: $T_h = 302.85$ K, $T_c = 293.35$ K. Geometric parameters of rotating copper plate: length $L = 160$ mm, width $= 120$ mm, thickness $= 5$ mm. The temperature amplitude of the first layer is subsequently measured at Ω of 0, $\frac{\pi}{16}$ rad s^{-1}, $\frac{\pi}{8}$ rad s^{-1}, $\frac{\pi}{5}$ rad s^{-1}, $\frac{\pi}{4}$ rad s^{-1}, $\frac{\pi}{3}$ rad s^{-1}, $\frac{2\pi}{5}$ rad s^{-1} and $\frac{\pi}{2}$ rad s^{-1}, respectively.

Parameters (triple-layer)
$T_0 = 298.15$ K, $A = 100$ K, $b = 0.005$ m, $d = 0.022$ m, $R = 0.055$ m, $\kappa_{c1}(\kappa_{c2}) = 165$ W m^{-1} K^{-1}, $\rho_{c1}(\rho_{c2}) = 8900$ kg m^{-3}, $c_{c1}(c_{c2}) = 390$ J kg^{-1} K^{-1}, $\kappa_r = 95$ W m^{-1} K^{-1}, $\rho_r = 7900$ kg m^{-3}, $c_r = 460$ J kg^{-1} K^{-1}, $\omega = \frac{\pi}{4}$ rad s^{-1}.

Simulation
Theoretical calculation and data processing are implemented in MATLAB®. Finite element analysis is performed in commercial finite-element software COMSOL Multiphysics® with the heat transfer module.

Simulation process
Firstly, establish the geometric model in the software. Secondly, set the time-dependent temperature equation $T = T_0 + A\cos(k_x x - \omega t)$ on the lower surface of the bottom layer. The remaining parts are automatically thermal insulated. Then set convective velocity Ω_1 for the double-layer simulation or Ω_1, Ω_2 for the triple layer simulation. Lastly, set the simulation time step and total transient simulation time, and extract the time-domain data for the calculation of temperature amplitude in the transient simulation solver.

Experimental setup
The temperature fields are measured by the infrared cameras Fotric 628 C and Fotric 347. To minimize thermal emissivity-induced errors, the observation surface is uniformly coated with graphene spray (thermal emissivity ≈ 0.98), ensuring consistent radiative properties during measurement.

Data availability
All relevant data are available from the corresponding author upon reasonable request.

Code availability
The code is available from the corresponding author Ying Li upon reasonable request.

References
1. Chen, Y., Wang, Z., Fan, Y., Dong, M. & Liu, D. Research Status and Progress on Non-Destructive Testing Methods for Defect Inspection of Micro-Electronic Packaging. *J. Electron. Packag.* **146**, 030801 (2024).
2. Kandwal, A. et al. Designing Highly Sensitive Microwave Antenna Sensor with Novel Model for Noninvasive Glucose Measurements. *Prog. Electromagn. Res.* **176**, 129–141 (2023).
3. Gupta, M., Khan, M. A., Butola, R. & Singari, R. M. Advances in applications of Non-Destructive Testing (NDT): A review. *Adv. Mater. Process. Technol.* **8**, 2286–2307 (2022).
4. Wu, K., Zhu, X., Zhao, X., Anderson, S. W. & Zhang, X. Conformal Metamaterials with Active Tunability and Self-Adaptivity for Magnetic Resonance Imaging. *Research* **7**, 0560 (2024).
5. Li, R. et al. Non-Invasive Self-Adaptive Information States' Acquisition inside Dynamic Scattering Spaces. *Research* **7**, 0375 (2024).
6. Breitenstein, O., Warta, W. & Schubert, M. C. *Lock-in Thermography: Basics and Use for Evaluating Electronic Devices and Materials*. vol. 10 (Springer International Publishing, Cham, 2018).
7. Li, Y. et al. Transforming heat transfer with thermal metamaterials and devices. *Nat. Rev. Mater.* **6**, 488–507 (2021).
8. Ju, R. et al. Convective Thermal Metamaterials: Exploring High-Efficiency, Directional, and Wave-Like Heat Transfer. *Adv. Mater.* **35**, 2209123 (2023).
9. Yang, F. et al. Controlling mass and energy diffusion with metamaterials. *Rev. Mod. Phys.* **96**, 015002 (2024).
10. Zhang, Z. et al. Diffusion metamaterials. *Nat. Rev. Phys.* **5**, 218–235 (2023).
11. Liu, J., Xu, L. & Huang, J. Spatiotemporal diffusion metamaterials: Theories and applications. *Appl. Phys. Lett.* **124**, 210502 (2024).
12. Alabastri, A. Flow-Driven Resonant Energy Systems. *Phys. Rev. Appl.* **14**, 034045 (2020).
13. Alabastri, A. et al. Resonant energy transfer enhances solar thermal desalination. *Energy Environ. Sci.* **13**, 968–976 (2020).
14. Ye, Q., Sanders, S. & Alabastri, A. Resonant Energy Transfer and Storage in Coupled Flow-Driven Heat Oscillators. *PRX Energy* **2**, 023007 (2023).
15. Wang, D., Chen, H., Qiu, C. & Li, Y. Non-Hermitian scattering symmetry revealed by diffusive channels. Preprint at https://doi.org/10.48550/arXiv.2303.13104 (2023).
16. Li, Y. et al. Anti-parity-time symmetry in diffusive systems. *Science* **364**, 170–173 (2019).
17. Cao, P.-C. et al. Observation of parity-time symmetry in diffusive systems. *Sci. Adv.* **10**, eadn1746 (2024).
18. Farhat, M., Guenneau, S., Chen, P.-Y., Alù, A. & Salama, K. N. Scattering Cancellation-Based Cloaking for the Maxwell-Cattaneo Heat Waves. *Phys. Rev. Appl* **11**, 044089 (2019).
19. Zhang, Z., Xu, L. & Huang, J. Controlling Chemical Waves by Transforming Transient Mass Transfer. *Adv. Theory Simul.* **5**, 2100375 (2022).
20. Li, Y., Li, J., Qi, M., Qiu, C.-W. & Chen, H. Diffusive nonreciprocity and thermal diode. *Phys. Rev. B* **103**, 014307 (2021).
21. Ordonez-Miranda, J., Guo, Y., Alvarado-Gil, J. J. & Volz, S. & Nomura, M. Thermal-Wave Diode. *Phys. Rev. Appl.* **16**, L041002 (2021).
22. Ordonez-Miranda, J., Anufriev, R., Nomura, M. & Volz, S. Net heat current at zero mean temperature gradient. *Phys. Rev. B* **106**, L100102 (2022).
23. Yan, H.-R., Cao, P.-C., Wang, Y.-X., Zhu, X.-F. & Li, Y. Geometric heat pumping under continuous modulation in thermal diffusion. Preprint at https://doi.org/10.48550/arXiv.2406.19100 (2024).
24. Wang, Z., Chen, J. & Ren, J. Geometric heat pump and no-go restrictions of nonreciprocity in modulated thermal diffusion. *Phys. Rev. E* **106**, L032102 (2022).
25. Li, Y. et al. Observation of heat pumping effect by radiative shuttling. *Nat. Commun.* **15**, 5465 (2024).
26. Ren, J., Hänggi, P. & Li, B. Berry-Phase-Induced Heat Pumping and Its Impact on the Fluctuation Theorem. *Phys. Rev. Lett.* **104**, 170601 (2010).
27. Ju, R. et al. Nonreciprocal Heat Circulation Metadevices. *Adv. Mater.* **36**, 2309835 (2024).
28. Xu, L., Huang, J. & Ouyang, X. Nonreciprocity and isolation induced by an angular momentum bias in convection-diffusion systems. *Appl. Phys. Lett.* **118**, 221902 (2021).

29. Xu, L., Huang, J. & Ouyang, X. Tunable thermal wave nonreciprocity by spatiotemporal modulation. *Phys. Rev. E* **103**, 032128 (2021).
30. Li, Y. et al. Heat transfer control using a thermal analogue of coherent perfect absorption. *Nat. Commun.* **13**, 2683 (2022).
31. Cao, P.-C., Peng, Y.-G., Li, Y. & Zhu, X.-F. Phase-Locking Diffusive Skin Effect. *Chin. Phys. Lett.* **39**, 057801 (2022).
32. Cao, P.-C. et al. Diffusive skin effect and topological heat funneling. *Commun. Phys.* **4**, 1–7 (2021).
33. Liu, Y.-K. et al. Observation of non-Hermitian skin effect in thermal diffusion. *Sci. Bull.* **69**, 1228–1236 (2024).
34. Huang, Q.-K.-L., Liu, Y.-K., Cao, P.-C., Zhu, X.-F. & Li, Y. Two-Dimensional Thermal Regulation Based on Non-Hermitian Skin Effect. *Chin. Phys. Lett.* **40**, 106601 (2023).
35. Wang, D., Ban, H. & Jiang, P. Spatially resolved lock-in micro-thermography (SR-LIT): A tensor analysis-enhanced method for anisotropic thermal characterization. *Appl. Phys. Rev.* **11**, 021407 (2024).
36. Švantner, M., Muzika, L., Chmelík, T. & Skála, J. Quantitative evaluation of active thermography using contrast-to-noise ratio. *Appl. Opt.* **57**, D49–D55 (2018).
37. Schmid, S., Reinhardt, J. & Grosse, C. U. Spatial and temporal deep learning for defect detection with lock-in thermography. *NDT E Int.* **143**, 103063 (2024).
38. Xiong, M. et al. Transmissive laser lock-in thermography for highly sensitive and online imaging of real interfacial bubbles in wafer bonding. *Infrared Phys. Technol.* **134**, 104903 (2023).
39. Iguchi, R., Fukuda, D., Kano, J., Teranishi, T. & Uchida, K. Direct measurement of electrocaloric effect based on multi-harmonic lock-in thermography. *Appl. Phys. Lett.* **122**, 082903 (2023).
40. Zhu, P., Wu, D., Wang, Y. & Miao, Z. Defect detectability based on square wave lock-in thermography. *Appl. Opt.* **61**, 6134 (2022).
41. Hirai, T., Ando, F., Sepehri-Amin, H. & Uchida, K. Hybridizing anomalous Nernst effect in artificially tilted multilayer based on magnetic topological material. *Nat. Commun.* **15**, 9643 (2024).
42. Breitenstein, O. & Sturm, S. Lock-in thermography for analyzing solar cells and failure analysis in other electronic components. *Quant. InfraRed Thermogr. J.* **16**, 203–217 (2019).
43. Mulaveesala, R. & Tuli, S. Theory of frequency modulated thermal wave imaging for nondestructive subsurface defect detection. *Appl. Phys. Lett.* **89**, 191913 (2006).
44. Uchida, K., Hirai, T., Ando, F. & Sepehri-Amin, H. Hybrid Transverse Magneto-Thermoelectric Cooling in Artificially Tilted Multilayers. *Adv. Energy Mater.* **14**, 2302375 (2024).
45. Łukaszuk, R. D., Marques, R. M. & Chady, T. Lock-In Thermography with Cooling for the Inspection of Composite Materials. *Materials* **16**, 6924 (2023).
46. Wang, F. et al. Multimode infrared thermal-wave imaging in non-destructive testing and evaluation (NDT&E): Physical principles, modulated waveform, and excitation heat source. *Infrared Phys. Technol.* **135**, 104993 (2023).
47. Liu, J. Y., Gong, J. L., Qin, L., Guo, B. & Wang, Y. Three-Dimensional Visualization of Subsurface Defect Using Lock-In Thermography. *Int. J. Thermophys.* **36**, 1226–1235 (2015).
48. Montinaro, N., Cerniglia, D. & Pitarresi, G. Evaluation of interlaminar delaminations in titanium-graphite fibre metal laminates by infrared NDT techniques. *NDT E Int.* **98**, 134–146 (2018).
49. Derusova, D. A., Vavilov, V. P., Guo, X. & Druzhinin, N. V. Comparing the Efficiency of Ultrasonic Infrared Thermography under High-Power and Resonant Stimulation of Impact Damage in a CFRP Composite. *Russ. J. Nondestruct. Test.* **54**, 356–362 (2018).
50. Song, J., Gao, B., Woo, W. L. & Tian, G. Y. Ensemble tensor decomposition for infrared thermography cracks detection system. *Infrared Phys. Technol.* **105**, 103203 (2020).
51. Bodnar, J. L., Nicolas, J. L., Candoré, J. C. & Detalle, V. Non-destructive Testing by Infrared Thermography Under Random Excitation and ARMA Analysis. *Int. J. Thermophys.* **33**, 2011–2015 (2012).
52. Wei, J., Wang, F., Liu, J., Wang, Y. & He, L. A laser arrays scan thermography (LAsST) for the rapid inspection of CFRP composite with subsurface defects. *Compos. Struct.* **226**, 111201 (2019).

Acknowledgements

Author contributions
Y.L. conceived the idea of the research. D.W., P-C.C. provided theoretical methodology. Y.W. performed theoretical numerical calculation, simulation, experiment, data analysis and wrote the draft. Y.W., D.W., P-C.C, X.X., Q-K-L.H. built the experimental platform. H-R.Y. contributed insightful comments to the draft. H.C. and Y.L. supervised the project. All the authors were involved in revising the paper.

Competing interests
The authors declare no competing interests.

Additional information
Supplementary information The online version contains supplementary material available at https://doi.org/10.1038/s42005-025-02207-w.

Correspondence and requests for materials should be addressed to Hongsheng Chen or Ying Li.

Peer review information *Communications Physics* thanks the anonymous reviewers for their contribution to the peer review of this work. A peer review file is available.

Reprints and permissions information is available at http://www.nature.com/reprints

Publisher's note Springer Nature remains neutral with regard to jurisdictional claims in published maps and institutional affiliations.